



SPE 123531

Maturity and Impedance Analysis of Organic-Rich Shales

Manika Prasad, SPE, Kenechukwu C. Mba, SPE, T. Elizabeth McEvoy, and Michael L. Batzle, SPE, Colorado School of Mines

Copyright 2009, Society of Petroleum Engineers

This paper was prepared for presentation at the 2009 SPE Rocky Mountain Petroleum Technology Conference held in Denver, Colorado, USA, 14–16 April 2009.

This paper was selected for presentation by an SPE program committee following review of information contained in an abstract submitted by the author(s). Contents of the paper have not been reviewed by the Society of Petroleum Engineers and are subject to correction by the author(s). The material does not necessarily reflect any position of the Society of Petroleum Engineers, its officers, or members. Electronic reproduction, distribution, or storage of any part of this paper without the written consent of the Society of Petroleum Engineers is prohibited. Permission to reproduce in print is restricted to an abstract of not more than 300 words; illustrations may not be copied. The abstract must contain conspicuous acknowledgment of SPE copyright.

Abstract

Organic-rich shales (ORS) need to be studied in detail to understand the provenance and the generation of oil from source rocks. In recent years, ORS have become interesting as important hydrocarbon resources as well. Successful exploration and production programs for ORS need reliable identification of the kerogen content and the maturity through indirect seismic methods. However, the seismic properties of kerogen are poorly understood and so, predictions about maturity and rock-kerogen systems remain a challenge. Assessment of maturity from indirect measurements can be greatly enhanced by establishing and exploiting correlations between physical properties, microstructure, and kerogen content.

In this paper we show correlations between the impedance microstructure of ORS and their maturity and elastic properties. We have used scanning acoustic microscopy to analyze and map the impedance microstructure in ORS. We quantified textural properties in the images and related these textural properties to maturity and to impedance from acoustic wave propagation measured at centimeter scales. This combined study of acoustic and microstructures of ORS give important insight in changes due to kerogen maturation. We introduce a modified porosity term and find that (i) there is a significant correlation between velocity and modified porosity of all ORS; (ii) Imaging and quantifying microscale impedance texture and contrast in the images allows us to correlate them with ultrasonic measurements on a cm-scale; and (iii) textural heterogeneity, elastic impedance, velocity, and density increase with increasing shale maturity.

In this paper, we show typical acoustic images of ORS and discuss possible methods to predict maturity from impedance based on understanding the changes due to maturity in well log response, core measurements, and microstructure of organic-rich shales. Our work has important bearing on developing successful production and stimulation methodologies.

Introduction

Organic-rich shales (ORS) and oil shales (OS) are increasingly being studied in detail to understand the provenance and the generation of oil from source rocks. In recent years, they have gained importance as hydrocarbon resource rocks. Proven and recoverable oil reserves from ORS and OS account for about 33 trillion tons of shale and 68 billion tons of oil, respectively. Of these, the US alone has 3.3 trillion tons of shale (10% of proven reserves from oil shales) and 60 billion tons of oil (90% of total recoverable oil from shales) with the estimated U.S. OS and ORS reserves totaling 1.5 trillion barrels of oil (Hepbasli, 2004).

Successful exploration and production programs for ORS must rely on reliable identification of the kerogen content and its maturity through indirect seismic methods. The seismic properties of kerogen are poorly understood. Consequently, predictions of the seismic response of a rock-kerogen system and the kerogen maturity remain a big challenge. Kerogen maturity changes shale texture. For example, overpressure due to hydrocarbon generation can lead to microcracks and fractures in the matrix (Lempp et al., 1994). Assessment of maturity from indirect measurements can be greatly enhanced by exploiting any existing correlations between physical properties, microstructure, and kerogen content.

One way of looking at ORS is through acoustic analysis. Numerous authors have shown that kerogen content, and with it maturity, can be related to P-wave velocity, V_p (for example, Wert and Weller, 1982; Mraz et al., 1983; Weller and Wert, 1983; Passey et al., 1990; Vernik and Nur, 1994; Vernik and Landis, 1996; Vernik and Liu, 1997; Prasad, 2001; Prasad et al., 2002a). P-wave velocity data measured in the laboratory by Vernik (reported in Vernik and Nur, 1994; Vernik and Landis, 1996; Vernik and Liu, 1997), hereinafter called the Vernik dataset, show that V_p increases with increasing maturity, except in high-porosity shales. In high-porosity (low maturity) shales, V_p is better correlated with porosity. Within a single formation, the correlation between V_p and HI is reasonable and the scatter is greatly reduced (Figure 1 from Prasad et al., 2002a). In our study we will examine the Bakken formation and investigate their acoustic and optical microstructure. We will also compare

P- and S-wave velocities, V_p and V_s , respectively measured in the laboratory with sonic well log data. The velocity measurements have led to our better understanding of the maturity processes in ORS. By understanding the microstructures that lead to velocity variations with maturity, kerogen content, and temperature, we can increase efficiency and reliability of fracture models and better predict fracture placement.

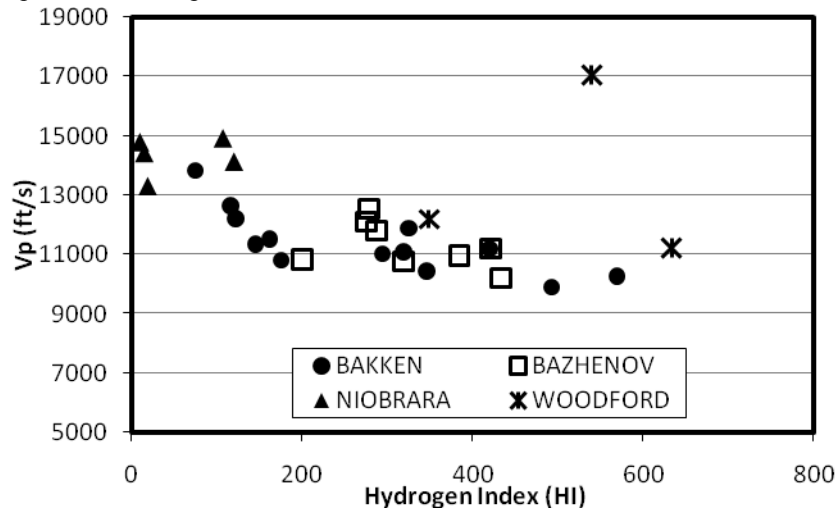


Figure 1. P-wave velocity (V_p in ft/s) versus Hydrogen Index (HI). Lower HI corresponds to higher maturity. From the figure, it is seen that V_p is inversely proportional to HI and directly proportional to maturity. There is a marked increase in V_p as HI decreases below 200. The figure is adapted from Prasad et al., 2002a.

Description of Equipment and Samples Used

Our experimental techniques were based on the pulse transmission of acoustic waves through samples of known length. In one experiment, V_p and V_s were measured and the elastic moduli were derived from them. Sonic velocity data were also used from well logs from published sources. In the acoustic imaging experiment, we recorded the reflections of acoustic waves at each position on the sample in a raster described below in detail.

Samples Used

We have used various ORS samples for our study. The Vernik dataset belonged to the Bakken Formation from the Williston basin, North Dakota, Bazhenov Formation from Western Siberia, Woodford Formation from Oklahoma, Niobrara Formation from New Mexico, Monterey Formation from California, and Locketong Formation from New Jersey. We imaged the samples with acoustic methods. Using scanning acoustic microscopy, we measured the impedance changes by scanning across the samples using compressional waves. The acoustic imaging was made at high (GHz-range) and low (MHz-range) frequencies. Some initial studies were done on core samples of the Bakken formation from North Dakota.

Scanning Acoustic Microscopy

The acoustic images were made with a scanning acoustic microscope (SAM) manufactured by Leica, Wetzlar, and upgraded by Krämer Scientific Instruments in Herborn, both of Germany. We have used SAM at 1 GHz to measure impedance in various rocks, for example sandstones and shales. A complete description of the application of scanning acoustic microscopy to petrophysics can be found in Prasad (2001) and Prasad et al. (2002a). Here we describe only main principles.

SAM can be best understood as microscopic analogs to side-scan sonar, zero-offset reflection seismic mapping, or ultrasound sonography. The main principle is to study surface and sub-surface features with the help of high-frequency acoustic waves. Images of surface and sub-surface microstructures are prepared on the basis of reflected acoustic waves that depend on the impedance changes in the sample. Acoustic waves that are incident on a sample are mode converted, partly transmitted into the sample, and partly reflected. The signal intensity received back at the transducer is governed by changes in acoustic impedance and hence by changes in the elastic constants of the material.

Three basic types of scans can be obtained from SAM:

1. An X-t scan (t = time) or an A-scan. This one dimensional A-scan is the primary information received at the transducer. An analog to reflection seismic would be a seismic line trace. The A-scan shows variations in signal amplitude with time received at a fixed lens position.
2. An X-Z scan or a B-scan. In analogy to a reflection seismogram, recording several A-scans (seismic traces) along a line makes a B-scan. Any layering, alignment of grains and pores, clusters of grains with same impedance can be mapped by these vertical two-dimensional scans.

3. An X-Y scan or a C-scan. This is a horizontal two-dimensional scan, similar to a side-scan sonar image. It is created by gathering information at a fixed time position on the A-scan and moving the lens in X and Y directions. Data obtained at time $t < 0$ gives the image of a subsurface layer.

SAM results of kerogen rich shales were obtained with a high-frequency (0.2 – 2 GHz) and a low-frequency (10 - 50 MHz) acoustic microscope both operating in reflection mode. The depth of penetration and resolution of microstructural features depend on the operating frequency. The 1 GHz high frequency lens was used for high resolution of about 1 μm with a scan area of $1 \times 1 \text{ mm}^2$. At frequencies in the GHz range, the opening angle of the acoustic lens is optimized to achieve a high sensitivity to surface acoustic (Rayleigh) waves. This design allowed us to map microstructural features from the interference patterns between normally reflected longitudinal waves and the Rayleigh waves (Briggs, 1992). MHz-range low frequency lenses were used for low resolution of about 30 μm with larger (cm scale) scan areas. These scans allowed us to map large-scale microstructural features from the normally reflected longitudinal waves.

C-scans of surface and subsurface features can be used to study impedance changes in the sample quantitatively. By making a gray scale calibration using materials of known impedance, the acoustic images of the rocks can be evaluated for impedance variations as functions of cementation strength, kerogen maturity, and reflectivity. To make a calibrated image, a set of standard materials is selected. The expected impedance in the unknown sample should lie within the impedance values of the standard materials. The standard samples are imaged at a fixed setting of signal and video gains, such that all samples can be imaged at that setting. The gray scale of each sample image is associated with its impedance and reflection coefficient with respect to the coupling medium, water. This gives rise to a calibration of the gray scale from 0 (= black) to 255 (= white), the depth of digitization in the SAM. Next, the unknown sample is first imaged at an optimum gain setting. Then, the gain setting is reverted to the calibration values and an image is recorded. The gray scale variations in the unknown image can then be determined from the calibration plot of reflection coefficient versus impedance based on a least-square fit. Approximately 10-15% error is to be expected due to instrumental drift, especially if calibrations are not performed often or if the sample has large variations in surface topography. The calibration procedure and calibration samples are described in Prasad (2001) and Prasad et al. (2002a). In this study, only the high frequency acoustic images were made with calibrated gray scales.

At low frequencies, depth information can be obtained by focusing the acoustic waves below the surface of the sample. The signals received back at the lens will then contain information about the entire path, from the surface to the focal point inside the sample. Such images are called defocussed images. Figure 2 shows a typical acoustic image of a USD 0.25 coin with the surface image created from acoustic reflections in Figure 2a. The corresponding defocussed image at a depth of 2 mm is displayed in Figure 2b. The “tails” imprint of the coin is seen together with the surface information. Such images can be very useful to obtain information about any cracks, fractures, and subsurface inhomogeneities.



Figure 2. Scanning Acoustic Image of a quarter. (a) shows a surface image and (b) was obtained by focussing about 2 mm (300 nanoseconds) into the coin. Note that in (b) the structure from the bottom of the coin (tails part) is clearly visible.

In this paper, we will show acoustic images of the Bakken formation obtained with GHz and MHz acoustic lenses. We will then relate them to acoustic measurements made on the samples at a cm-scale. Since the microstructural information is also obtained from impedance contrasts, any changes in seismic velocities will be related to microstructural changes. In this manner, we explore causes for seismic velocity changes due to maturity (Prasad et al., 2002a).

Pulse Transmission Experiments

The acoustic Vp and Vs data taken from the Vernik dataset were measured in pulse transmission mode. The data set contains information on Vp and Vs measured in three different directions, stiffness moduli for a transversely isotropic system, hydrogen index, volumetric kerogen content, porosity, and density.

Presentation of Data and Results

Organic-rich shales were studied under a scanning acoustic microscope to understand their microstructural properties and the causes for the elastic anisotropy. Acoustic microscopy allows us to map the impedance microstructure of samples using reflected acoustic waves. Three sets of samples were studied from various stages of kerogen maturation: diagenesis, catagenesis, and metagenesis. Microstructural and impedance differences are observed as the shales undergo the different stages of maturation. These changes can be related to the velocity anisotropy measured with ultrasonic pulse transmission methods.

Acoustic Images at MHz-frequencies

In the low (MHz) frequency SAM system, the microstructural properties are studied from reflection of longitudinal waves at various interfaces in the sample. Normally reflected longitudinal waves contribute toward the impedance information on the sample. In the low frequency acoustic images, two types of scans are obtained, a C-scan and a B-scan. The C-scan gives us a surface or sub-surface image and the B-scan a zero-offset reflection profile. In analogy to reflection seismic mapping, reflections occur at interfaces where the waves encounter an impedance change. If this interface is continuous, it will be mapped as a layer in the B-scan. The layers can be mapped in three dimensions by combining multiple B-scans made at various locations on the sample and analyzed to map dips, subsurface cracks and faults.

The acoustic scans obtained at 15 - 50 MHz and at 1 GHz gave important insight into the changes in texture with maturity and depth. Changes in maturity are expected to be accompanied by changes in microstructure such as those documented during hydrous pyrolysis experiments by Lewan (1987). Prasad et al. (2002a) calculated that the ultrasonic velocity increases by about 20% from Stage II maturity (HI = 584) to Stage IV maturity (HI = 122) in the Bakken from the Vernik dataset.

The shale samples used for Vp (0) measurements were coated with varnish to prevent them from swelling on contact with water. They were then used for acoustic scanning experiments at 15 MHz. Acoustic B- and A-scans of an immature Woodford shale sample (7068 ft) are presented here in Figure 3, and SAM C-scan images are shown in Figure 4. The SAM C-scan images show representative impedance changes and can be used to understand the reflectivity patterns in the AS scans of Figure 3. The impedance change between the coarse grained layer (Figure 4, right) and the fine grained layer (Figure 4, left) gives rise to a strong reflection (Figure 3b). This reflector is not observed in the AS of the same sample made by turning the sample 180° (Figure 3a). The contact between the two layers is closer to the top here. The event is masked by the high reflectivity of the shale.

A three dimensional reconstruction of the B-scans from each side (Figure 5) demonstrates the continuity of the layers and the high reflectivity in the shale. Similar reconstruction of two Bakken shales (immature, 8630 ft and mature, 11246 ft) are shown in Figure 6 and Figure 7, respectively. Again, a similar pattern is observed. These patterns help explain the acoustic velocity anisotropy measured in pulse transmission experiments.

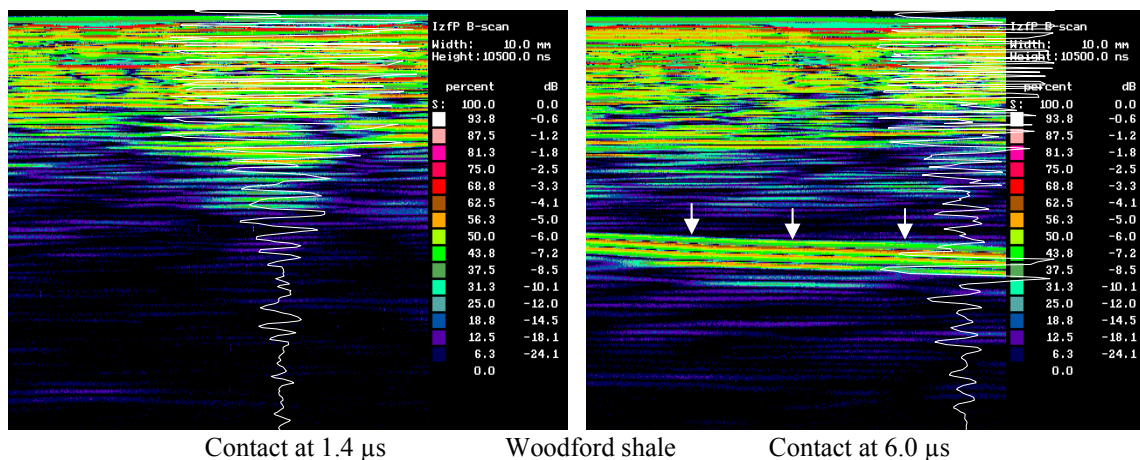


Figure 3. Acoustic sounding of an immature Woodford shale (7068 ft) at 15 MHz. Images are made of the same sample from opposite directions: Left image has the coarse grained, high impedance layer on top. The contact is at 5.5 mm (=1.4 μ s). Right image has the coarse grained, high impedance layer at the bottom. The contact is at 22.7 mm (=6 μ s) and gives rise to the prominent reflector marked by arrows. The corresponding impedance microstructure (Figure 20) shows two layers with an impedance change.

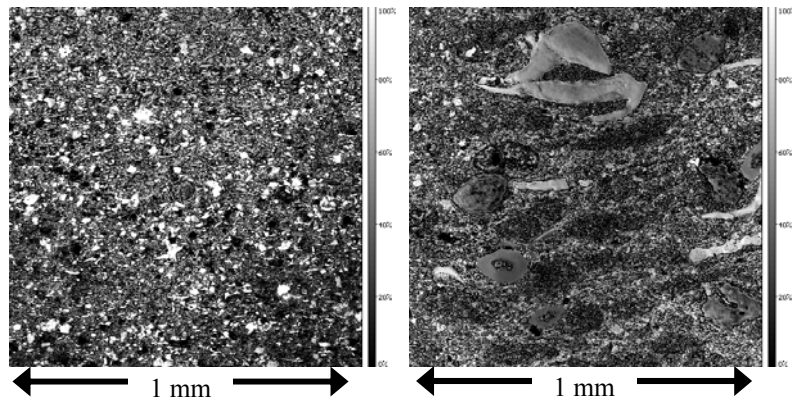


Figure 4. Acoustic images of an immature Woodford shale (7068 ft). The two images correspond to the different layers in the sample. One layer (left) has very low impedance and consists of fine grained, biogenic calcite debris in a matrix of kerogen material and some pyrite. The second layer (right) has aligned lenses of low impedance material (kerogen + pyrite) alternating with high impedance, coarser grained, biogenic (fishbone) calcite debris. The matrix here has intermediate impedance, between the kerogen + pyrite lenses and the organic debris. Note, the gray level in both images has been adjusted to make salient features readily visible.

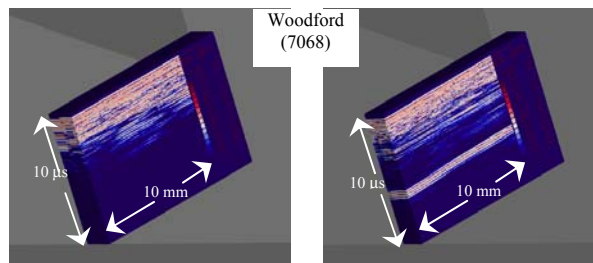


Figure 5. 3D images of the immature Woodford shale (7068 ft) from Figure 4. Images from 6-7 B-scans are combined to trace continuity of reflectors. The two images correspond to the same sample imaged from opposite directions, similar to Figure 4. In the left image, the coarse grained, high impedance layer faces up towards the transducer, and contact between layers is 5.5 mm ($=1.4 \mu\text{s}$) below the surface. The acoustic waves must first pass through the coarse grained layer with the pyrite-kerogen lenses before they hit the boundary. In the right image, the coarse grained, high impedance layer at bottom and contact between layers is 22.7 mm ($=6 \mu\text{s}$) from surface. Despite being further away from the surface than in the first case, the boundary gives rise to the prominent reflector seen towards the lower half of the image.

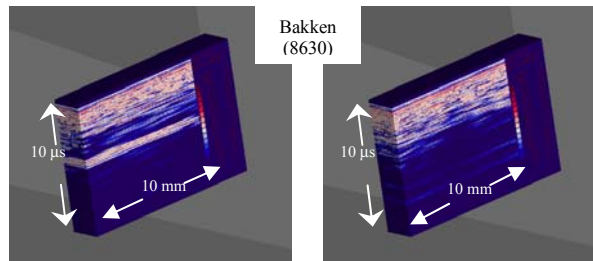


Figure 6. 3D images of the immature Bakken shale (8830 ft). Images are made from 6-7 B-scans combined to trace continuity of reflectors. The two images correspond to the same sample imaged from opposite directions: A layer in the top half of the left image is still seen in the lower part of the right image.

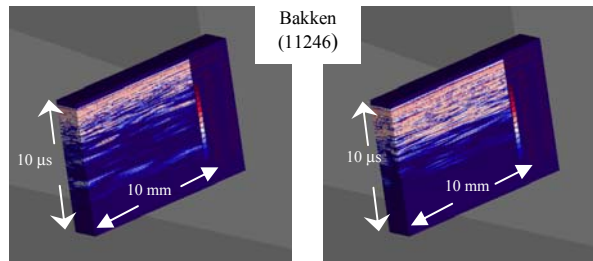


Figure 7. 3D images of the mature Bakken shale (11246 ft). Images are made from 6-7 B-scans combined to trace continuity of reflectors. The two images correspond to the same sample imaged from opposite directions. The various reflectors in both images are not continuous over a long distance.

Figure 8a shows a low frequency focussed image of a sample with sharp contrast between the Upper Bakken in the lower part of the image and the underlying Three Forks siltstone in the upper part of the image. The change in texture, along with the prevalence of micro-fractures in the upper part of the image emphasizes the change across the contact. Figure 8b is a zoomed in image from the lower part of Figure 8a showing the dark gray shades. This indicates lower impedances in the

kerogen-rich shale. Figure 8c is zoomed into the upper part of Figure 8a and shows lighter gray, higher impedance fractured zone above contact. Figure 9a, Figure 9b, and Figure 9c show samples with even finer grained matrix in contrast with Figure 8. These samples are below the resolution of the 50MHz transducer. Future work is planned with higher frequency transducers to improve the impedance imaging of these samples.

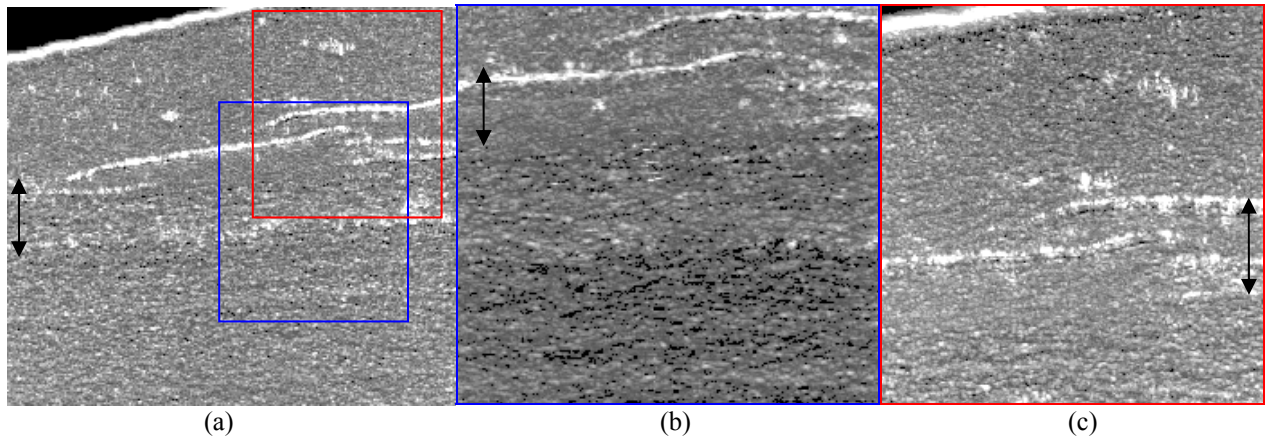


Figure 8 Acoustic image of a sample from Well Koch 2_28 made at 50 MHz. (a) shows an overview of the sample with the contact zone (marked by arrows) recognized by light bands and lighter grey shades. The image size is 20 mm x 17.8 mm. (b) A zoomed image of the area shown by the blue box in (a). Note that the image is darker gray below the contact zone indicating lower impedances. The image size is 11.8 mm x 10.8 mm. (c) A zoomed image of the area shown by the red box in (a). Note that the image is lighter gray above the contact zone indicating higher impedances. The image size is 9.4 mm x 8.9 mm.

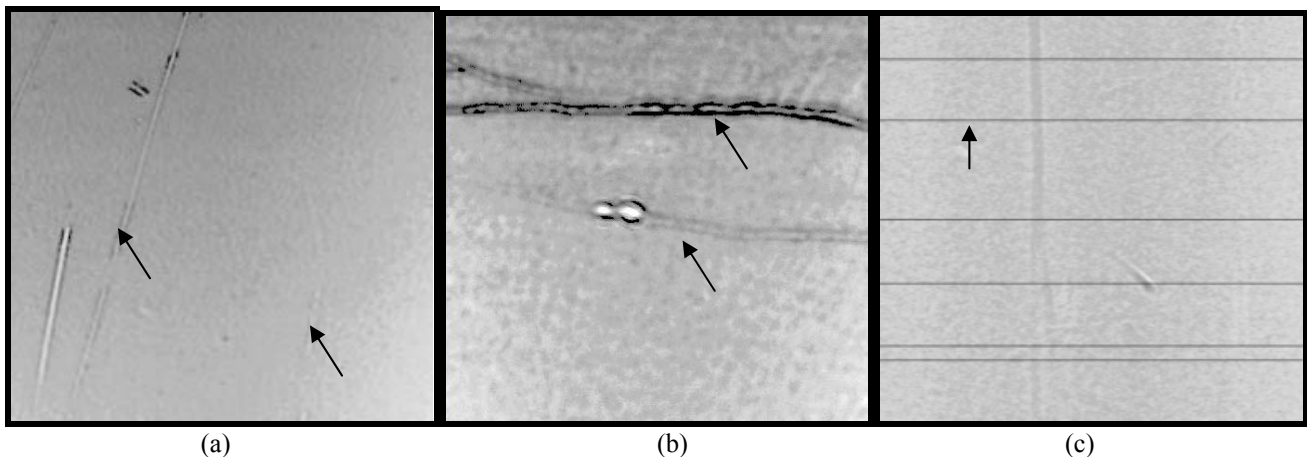


Figure 9. Acoustic image of a sample from Wells HG 21-26H and Koch 2-28 made at 50 MHz. (a) shows the sample HG 9052 with some scratches marked by arrows. The image size is 20 mm x 20 mm. (b) shows the sample HG9056 with horizontal fractures. The image size is 15 mm x 13.8 mm. (c) shows the sample K7030 with a very uniform texture. Note that the horizontal lines (parallel to the one marked by the arrow) are missing data and do not belong to texture. The image size is 15 mm x 40 mm.

Acoustic Images at 1 GHz

Despite similar chemical compositions, microstructure of the samples differed considerably. Acoustic micrographs of the Bakken shale series samples are shown in Figure 10 to Figure 12. These C-scan surface images were made at 1 GHz. All figures show acoustic scans of the Bakken shale at different magnifications; from an expanded view of 62.5 μm (left) to 1 mm (right). They are also arranged in order of increasing maturity from Figure 10 to Figure 12. In Figure 10, the black colored areas are mostly kerogen material, since there is very little porosity in the sample (< 5 %). White areas mark grains. The dark colors in the 312 μm image (Figure 10c) are a result of the acquisition as an impedance calibrated image showing very low impedance in the sample.

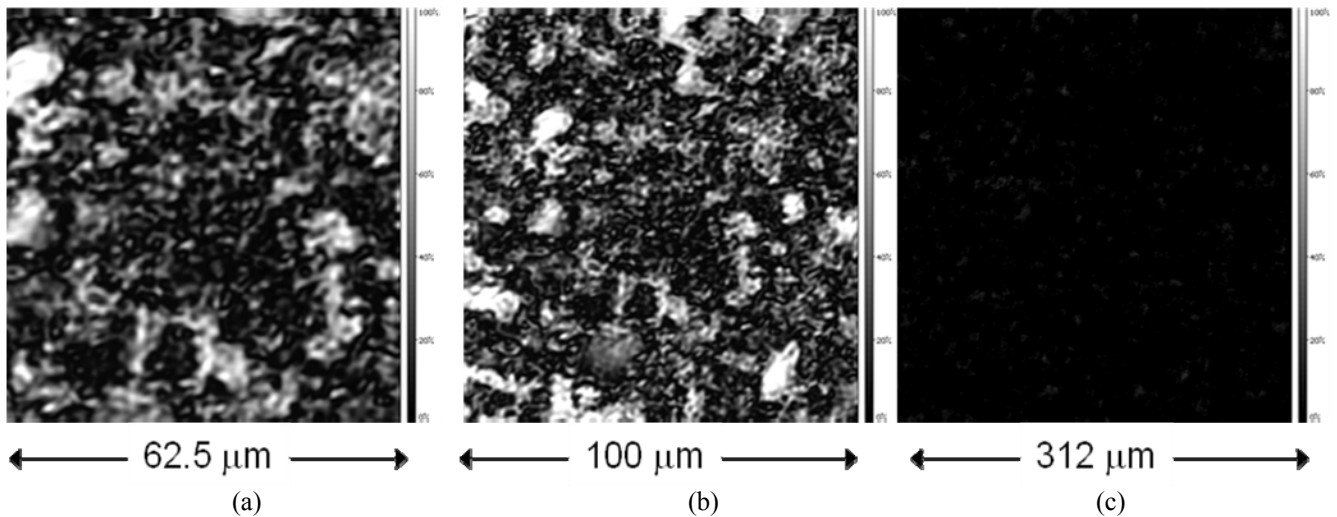


Figure 10. High frequency (1 GHz) scan of a low maturity Bakken shale from the Vernik study. The black colored areas are mostly kerogen material, since there is very little porosity in the sample (< 5 %). White areas mark grains. The dark (almost black) color of the image in (c) is a result of its acquisition with impedance calibration. The dark colors imply very low impedance in the sample.

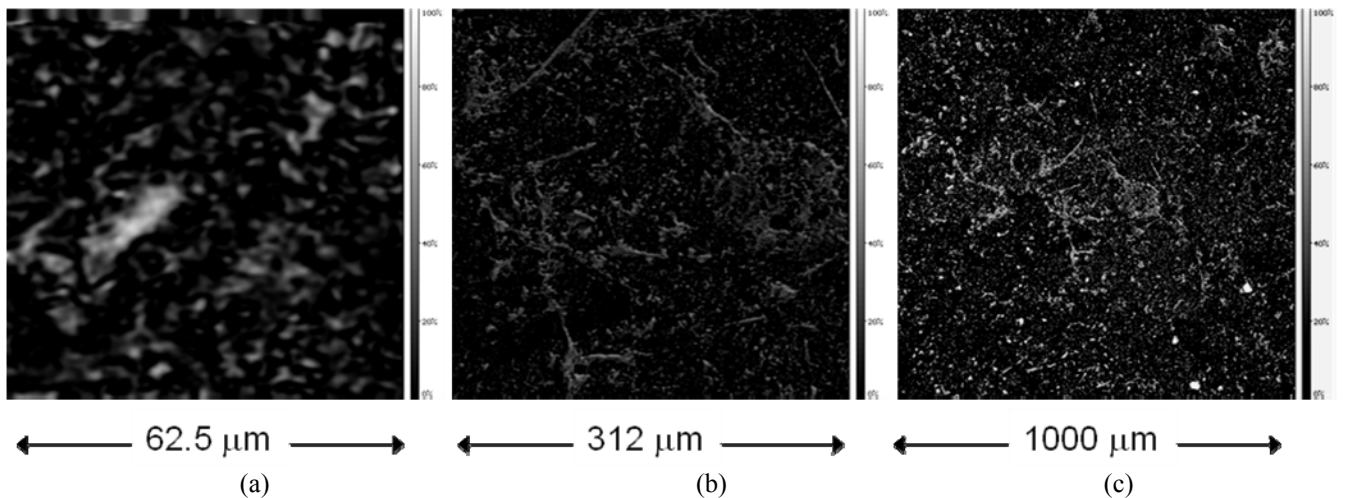


Figure 11. High frequency (1 GHz) scan of a medium maturity Bakken shale from the Vernik study. The black colored areas are mostly kerogen material, since there is very little porosity in the sample (< 5 %). White areas mark grains. Note the difference to Figure 10: the grains appear to form bridges (white-colored bands) across the kerogen material.

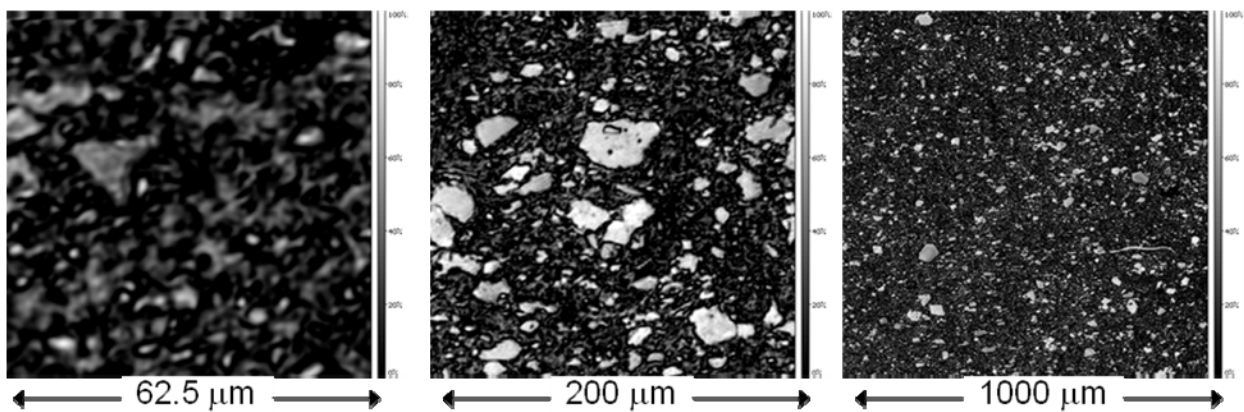


Figure 12. High frequency (1 GHz) scan of a high maturity Bakken shale from the Vernik study. The black colored areas are mostly kerogen material, since there is very little porosity in the sample (< 5 %). White areas mark grains. Note the difference to Figure 10 and Figure 11: the texture is much coarser grained (white-colored areas) and the kerogen (black-colored areas) appears in pockets within the grains.

From the different maturity shale samples examined in this study, we find following major differences in the impedance microstructural images:

- Inverse relation between kerogen content, maturity, and impedance

- Increase in grain size and in the number of coarse grains in mature shales
- Major change in kerogen and grain distribution with maturity: In immature shale, kerogen forms a more or less connected matrix and the higher impedance grains are dispersed in this matrix. In more mature shale, there is a significant increase in number of coarse grains and the grains form a framework with kerogen distributed in the pore space.

In the high frequency images, we assume that all lowest impedance areas are organic matter. Impedance properties of kerogen are not well known, but we expect it to have the lowest value among all other constituents. Zeszotarski et al. (2004) determined the nanoindentation modulus of kerogen in Woodford shale to be 11 GPa. This modulus value is close to that of a clay-water system (Prasad et al., 2002b). Thus, by mapping the lowest impedance in these clay-poor shales, we expect to map the relative location of the kerogen in the shales.

The microstructure has important applications for the mapping changes in stiffness and impedance of the shales with changing maturity. Lower maturity organic materials containing a large proportion of aliphatically associated hydrogen tends to have lower density and to deform plastically under load, whereas organic matter with less hydrogen (i.e., higher maturity) has higher density and lower plasticity (Smith and Chong, 1984). Thus, the lower maturity shales with load-bearing organic matter will deform plastically. On the other hand, as the organic matter gets more and more confined to pores, the rock will become stiffer and brittle and could be identified by higher velocities.

Since the amount and location of the organic matter changes with maturity, seismic attenuation could be used to map such changes. Internal friction measurements as functions of temperature in coal and ORS show three peaks corresponding to relaxation mechanisms in the kerogen (Wert and Weller, 1982; Weller and Wert, 1983). The temperature variation of velocity (either due to maturation in the natural case or due to pyrolysis in the laboratory) could be due to progressive effects with temperature increase of water loss from the shales, pyrolysis of the kerogen, and finally cementation of shale matrix by the pyrolysis products (Mraz et al. 1983). This progressive cementation with maturity is also seen in the acoustic images as described above.

Velocity Analysis

The data set was analyzed for any correlations between velocity and kerogen content. Such a correlation would help to develop prediction methods using indirect seismic or well log measurements. Figure 13 shows first a density – porosity correlation. The effect of kerogen porosity must be taken into consideration when developing such relations. Similarly, the velocity relation with porosity or kerogen content is not as good (Figure 14). Within each formation, the velocity – porosity correlation is good, but any general prediction of kerogen content not based on site-specific velocity trends would have large errors.

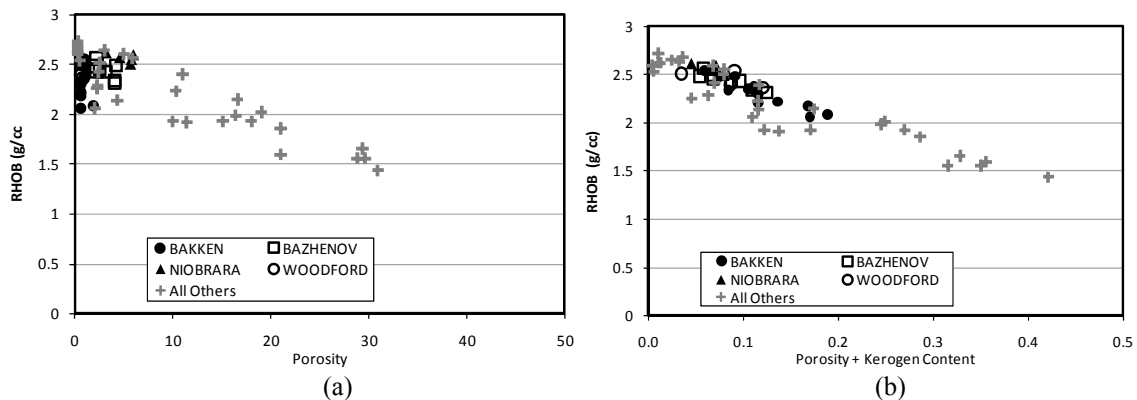


Figure 13. Density – Porosity correlation (a) becomes much better if we modify the total porosity by adding the contribution of kerogen content to the porosity (b). In the analysis, we have assumed the kerogen porosity to be 40%.

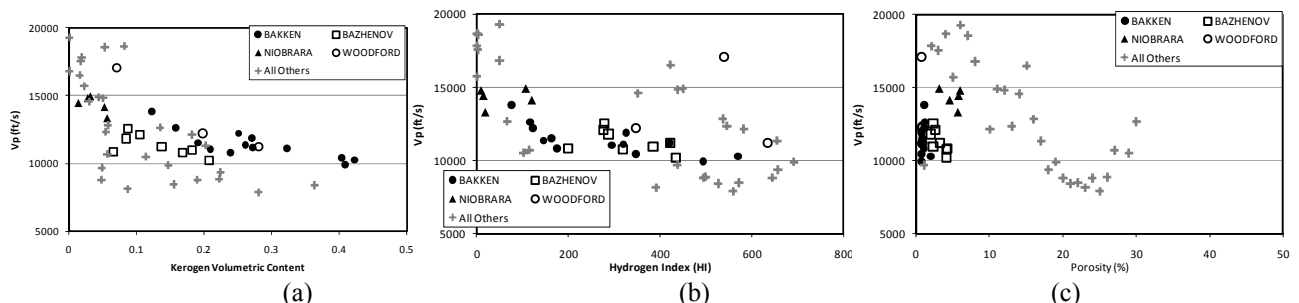


Figure 14. Velocity does not correlate very well with kerogen volumetric content (a), with Hydrogen Index (b), and porosity (c). Note that within any given formation, there is a fairly good correlation.

The scatter in the velocity data in Figure 14 and the lack of its correlation with porosity and kerogen content could be explained by the fact that although most kerogen shales have low porosity, some do have significant pore space. Furthermore, not all of the kerogen is load-bearing. Since presence of both kerogen and porosity lead to velocity reduction, we define a porosity - modified kerogen content by adding total porosity to the kerogen porosity. We arbitrarily assumed that about 40% of the kerogen acts similar to porosity and softens the rock. Thus we add to the total porosity a 40% contribution from kerogen content. Not only is the correlation coefficient now significantly higher, the correlation between velocity and porosity - modified kerogen content is vastly improved and encompasses all formations (Figure 15).

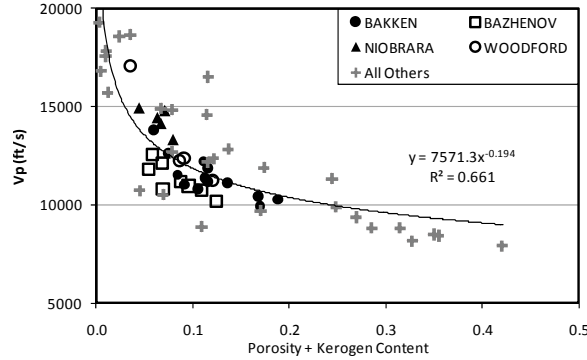


Figure 15. Velocity correlates very well with kerogen volumetric content if we assume that about 40% of the kerogen acts as pore space to soften the rock. Thus, we add a 40% contribution from kerogen content to the total porosity. The correlation coefficient between velocity and porosity - modified kerogen content is now significant ($R^2 = 0.7$) and does not depend on formation.

For a number of applications, the elastic moduli and strength parameters of the rocks are needed. We investigated effect of the porosity - modified kerogen content on the C11 and C33 stiffnesses (Figure 16) and on the C44 and C66 stiffnesses (Figure 17) as functions of the modified porosity. The C11 and C33 stiffnesses are derived from V_p measured parallel and perpendicular to any textural alignments and the C44 and C66 stiffnesses are derived from V_s measured parallel and perpendicular to the textural alignments. Also, the correlation coefficient between velocity and modified porosity is now significantly higher ($R^2 = 0.8$ and 0.9 for C11 and C66, respectively).

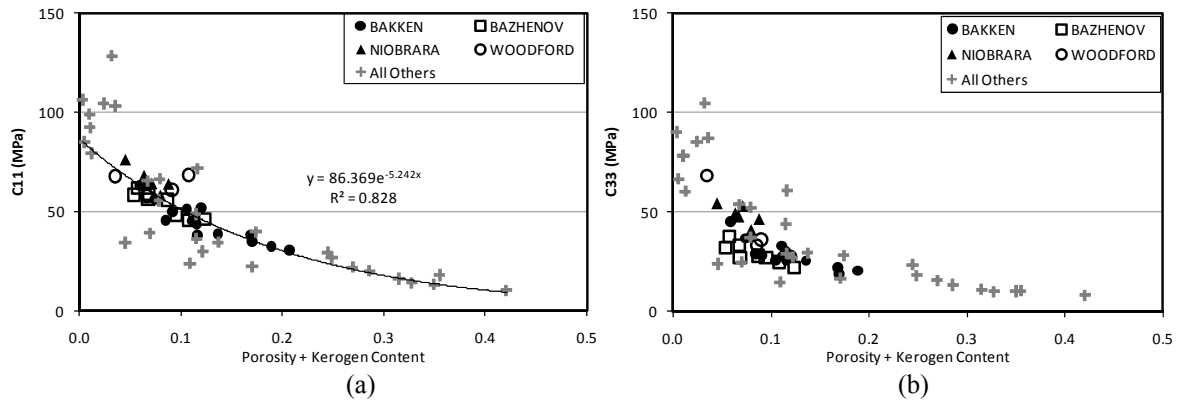


Figure 16. Elastic moduli (C11 in (a) and C33 in (b)) correlate very well with kerogen volumetric content modified by total porosity. As in Figure 15, we have assumed the kerogen porosity to be 40%. The C11 and C33 moduli are related to $V_p(90)$ and $V_p(0)$, respectively. The correlation coefficient is even higher than for velocity (in a, $R^2 = 0.8$ for C11).

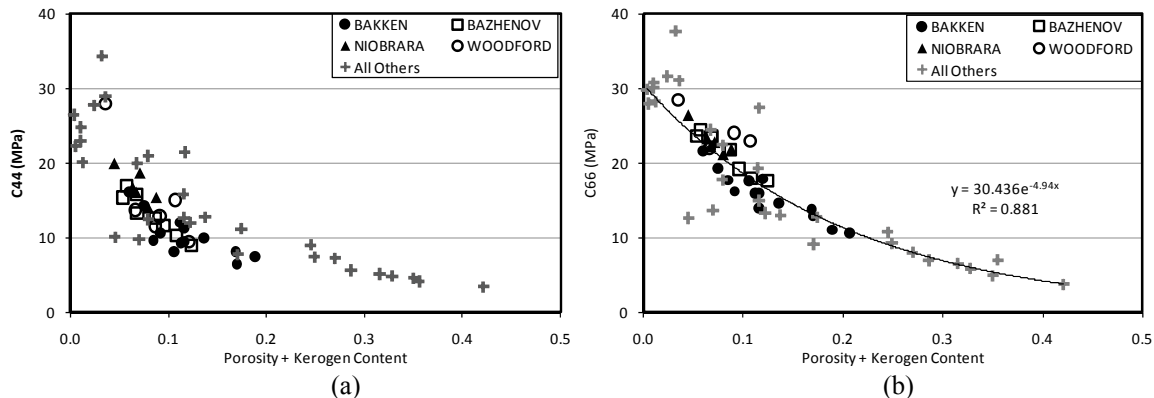


Figure 17. Elastic moduli (C44 in (a) and C66 in (b)) correlate very well with kerogen volumetric content modified by total porosity. As in Figure 15, we have assumed the kerogen porosity to be 40%. The C44 and C66 moduli are related to $V_{sh}(90)$ and $V_s(0)$, respectively. The correlation coefficient is even higher than for velocity (in b, $R^2 = 0.9$ for C66 = $30.436e^{-4.94 \text{ modified kerogen}}$).

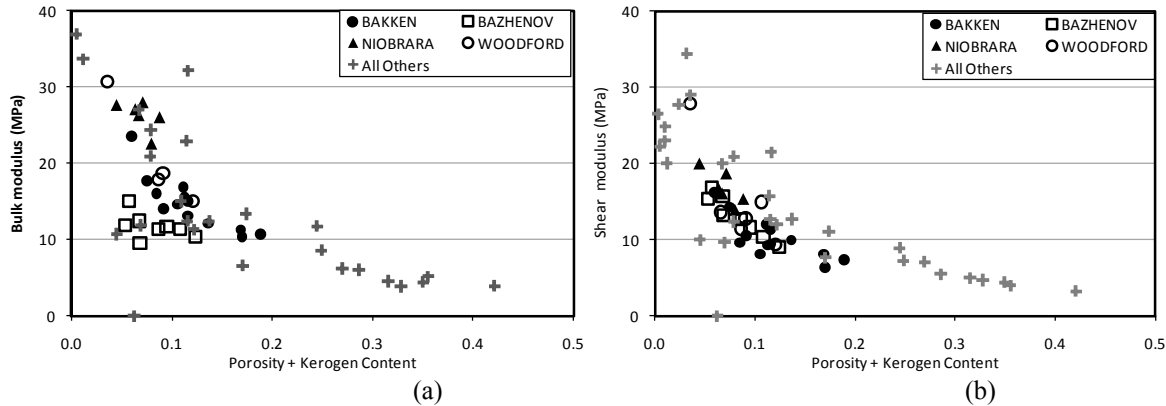


Figure 18. Bulk (a) and shear (b) moduli as functions of the modified porosity. As in the stiffnesses, there is a significant inverse correlation of the moduli with the porosity - modified kerogen content.

Comparison with log data

The P- and S-wave velocities (V_p , V_s , respectively) measured in this study were compared with the Vernik dataset and with well logs reported in Meissner (1978). Figure 19 shows a comparison of all velocity data. A constant overburden density was assumed in deriving confining pressure for this comparison. Interval transit time, DT in Figure 19a and V_p in Figure 19b show similar general trends of increasing velocity with depth. Two outliers plot at just over 12,000ft/s. The first is from a sample at 7,017ft with pyrite inclusions and the other is from the shale sample at the contact with the underlying siltstone formation at a depth of 7,038ft.

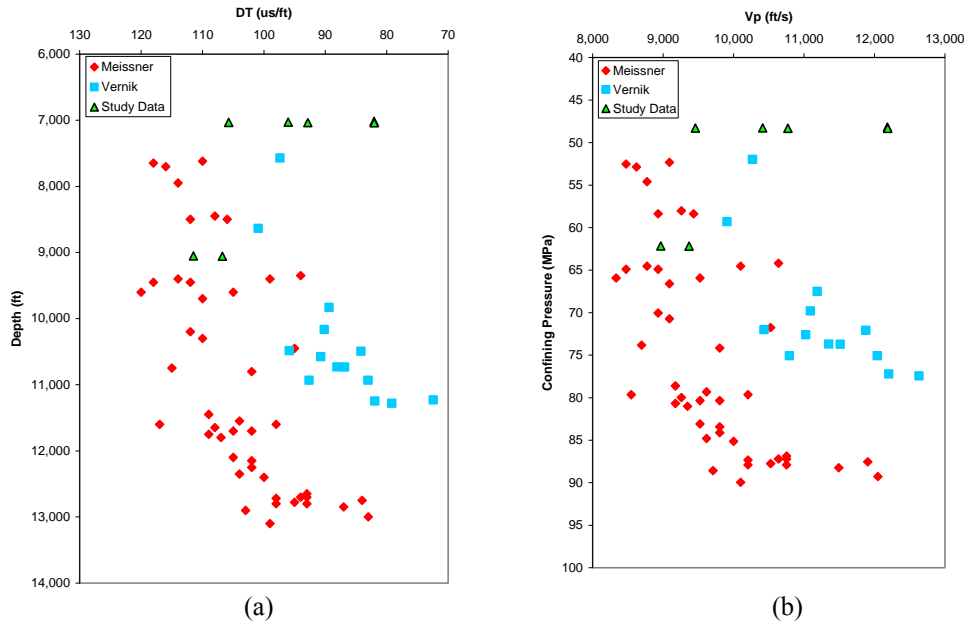


Figure 19. DT as a function of depth (a) and the same data expressed in V_p as a function of pressure (b). The depth was converted to pressure assuming a constant density in the overburden. Note that the Vernik data (squares) set shows consistently higher velocities than the well log data (diamonds) from Meissner (1978) and the data collected in this study (triangles).

The difference between laboratory measured velocities and sonic logs could have many reasons. The most obvious is that of pressure: sonic logs are measured at in situ whereas our laboratory values were derived at room conditions. The data from Meissner (1978) were from down-hole sonic logs and thus are at in situ pressures; the Vernik velocity data were measured at a confining pressure of 70Mpa, while data from this study were collected at ambient conditions. A relative comparison can however be made showing that Vernik's data is consistently higher than the well log data and data from this study. Further investigation is planned in this study to include velocity measurements with varying pressures and maturity.

A few other most common sources of discrepancy are sample size:

1. Size bias: Laboratory measurements are made on cm-sized core plugs; sonic logs are made on m-sized rock intervals.
2. Sampling bias: core plugs are often taken away from visible fractures and so are biased towards intact rock. Sonic logs measure the in situ properties.

3. Frequency difference: Laboratory measurements are mostly made at MHz-range. Sonic logs are made at kHz-range. Laboratory values can be higher than sonic logs due to dispersion effects. Jones and Wang (1981) predicted ultrasonic velocities to be 4% higher than sonic velocities as a result of dispersion in the Williston basin shales.
4. Difference due to variations in sampling and shale maturity.

Figure 20a shows a large scatter in shear-wave velocity data with no particular trend with depth. At depths below 10,000ft, however, an argument can be made for a trend showing increasing shear-wave velocity with depth. Velocity anisotropy on the other hand shows no trend at any depth as shown in Figure 20b. Anisotropy is as high as 20 percent in some samples with no apparent change with depth. This observation is similar to the one derived from the Vernik dataset where V_p - and V_s -anisotropy remained constant with maturity and pressure.

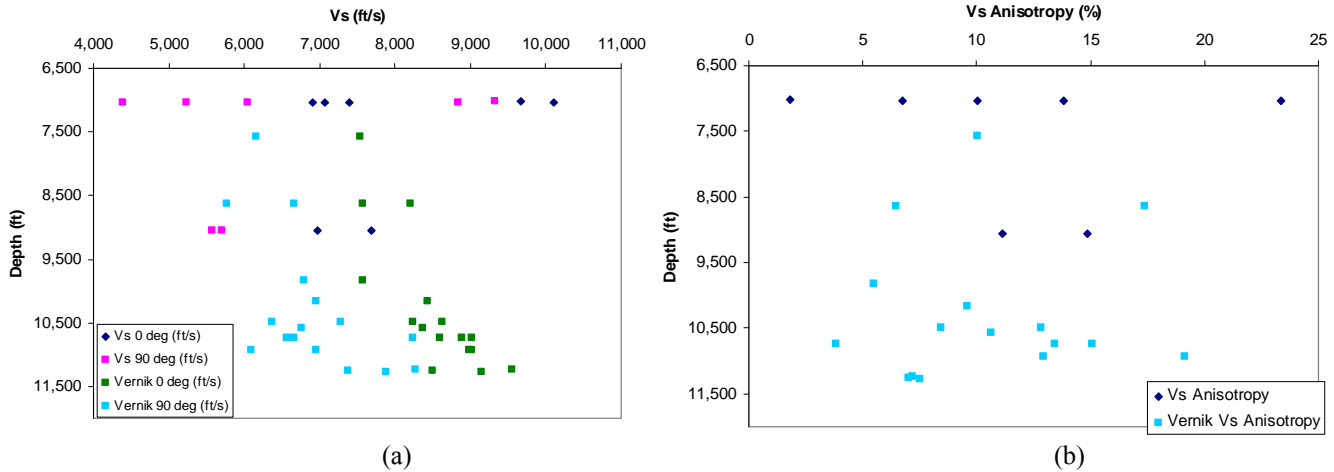


Figure 20. Shear wave velocity (V_s) (a) and shear wave anisotropy (b) versus depth compared with the Vernik data set. Note the large scatter in data at each depth. V_s varies between 4500 – 10,000 ft. Anisotropy can be as high as 20 %. Note that there is no apparent decrease in anisotropy with depth.

Fracture and Strength Considerations for Production Scenarios

Given their minimal porosity, any production mechanism in these organic-rich shale formations would need an understanding of their fracture mechanism. Experimental studies have shown that static compressive strength is dependent on the kerogen content (see Lankford, 1976 for comparison). Similar to the elastic moduli (Figure 18), an increase in total organic content tends to decrease compressive strength. With increasing temperatures, higher TOC shale samples deform predominantly plastically and pore pressure buildup leads to tensile microfractures (Lempp et al. 1994). This has important bearing on planning successful production scenarios, since hydrofracturing techniques rely on elastic moduli and porepressure build up, and in situ processing employ some kind of retorting.. In order to make reliable estimates of pore pressure buildup and effective stresses, we present the Biot’s coefficient calculated for the Vernik dataset (Figure 21). Biot’s coefficient (α) is calculated from the measured bulk moduli (K) and assuming a grain modulus (K_s) = 71 GPa (for carbonates) using $\alpha = 1 - (K/K_s)$. This parameter allows us to calculate the effective stress acting on the rock matrix ($P_{eff} = P_{ob} - \alpha P_p$).

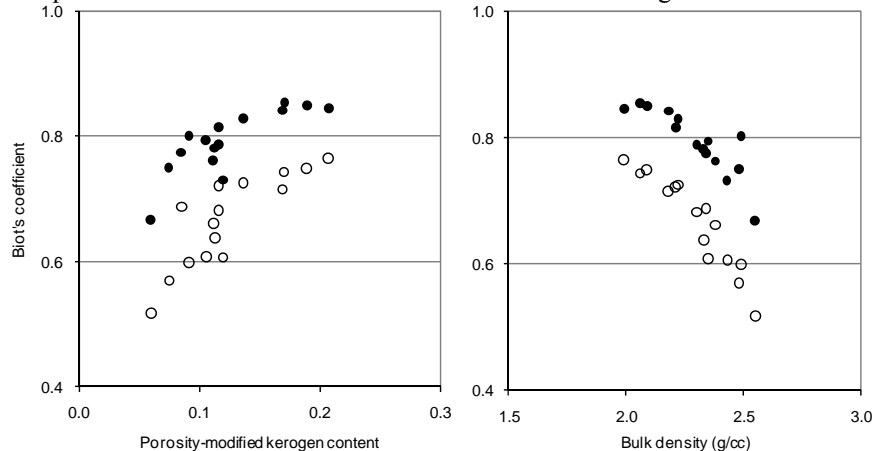


Figure 21. Biot’s coefficient for the fast (solid circles) and the slow (open circles) directions calculated for the Vernik dataset as functions of porosity-modified kerogen content (a) and bulk density (b). A few observations can be made from these figures: Biot’s coefficient is less than 1 and is inversely proportional to maturity, decreasing to below 0.6 for mature ORS. The magnitude of anisotropy in Biot coefficient is high and remains constant regardless of kerogen content.

A few key observations critical to future planning can be made from Figure 21:

1. The Biot's coefficient is less than 1 and is inversely proportional to maturity, decreasing to below 0.6 for mature ORS. Any in situ pyrolysis to generate pore pressures as well as hydraulic fracture stimulations will need to take these low Biot coefficients into consideration. Furthermore, the stimulation scheme would also need to be adapted to maturity level of the formation.
2. The magnitude of anisotropy in Biot coefficient is high and it remains constant regardless of kerogen content. In Figure 21, open circles are values derived from measurements perpendicular to bedding (slow direction) while solid circles are derived from measurements parallel to bedding (fast direction). In continuation of Point 1, the stimulation planning will need to address the prevalent formation anisotropy.

Conclusions

We find:

1. The correlation between kerogen content and elastic properties is significantly better if we use porosity-modified kerogen content and assume a kerogen porosity equal to 40%.
2. An inverse correlation between stiffness and modified porosity kerogen content. For example, the C66 stiffness can be predicted by $C66 = 30.436e^{-4.94 * \text{modified kerogen}}$, with an $R^2 = 0.9$.
3. Increase in grain size and in the number of coarse grains in mature shales
4. Major change in kerogen and grain distribution with maturity: In immature shale, kerogen forms a more or less connected matrix and the higher impedance grains are dispersed in this matrix. In more mature shale, there is a significant increase in number of coarse grains and the grains form a framework with kerogen distributed in the pore space.
5. The Biot's coefficient is less than 1 and is inversely proportional to maturity, decreasing to below 0.6 for mature ORS.

Ultrasonic imagery using scanning acoustic microscopy was successful in characterizing the kerogen content and maturity of organic-rich shales. Integration of impedance data from these measurements with observations from optical microscopy and down-hole sonic data can lead to useful correlations for detecting shale maturity through indirect surface measurements. In this study, relationships have been established between velocity and porosity, and between velocity and kerogen content. Future formation-specific evaluation work is planned for integration of the evolution of micro-fractures during the course of maturity with microstructural texture variation, kerogen content and shale maturity.

Acknowledgments

We thank Lev Vernik for his suggestion to investigate organic rich shales and his valuable input. This work was supported by a grant from DOE (Award#: DE-NT0005672) and by the Direct Hydrocarbon Indicator / Fluids consortium at Colorado School of Mines. The GHz-range and some MHz-range images were made using the acoustic microscope facilities of the Fraunhofer Institute for Nondestructive Testmethods (IzfP) in Germany for the acoustic microscope studies. MP thanks the IzfP and Walter Arnold for allowing usage of their facilities so freely.

References

- Briggs, G. A. D., 1992, *Acoustic Microscopy: Monographs on the Physics and Chemistry of Materials*, 47, Oxford Science Publications.
- Hepbasli, A., 2004, Oil Shale as an Alternative Energy Source: *Energy Sources*, 26:107–118, 2004; DOI: 10.1080/00908310490258489
- Jones, L. E. A., Wang, H. F., 1981, Ultrasonic velocities in Cretaceous shales from the Williston basin: *Geophysics*, v. 46, no. 3, 288-297.
- Lankford Jr., J., 1976, Dynamic Strength of Oil Shale: *Society of Petroleum Engineers Journal*, Paper (SPE 5327).
- Lempp, Ch., Natau, O., Bayer, U., Welte, D.H., 1994, The effect of temperature on rock mechanical properties and fracture mechanisms in source rocks - Experimental results, paper SPE 28039 presented at the 1994 SPE/ISRM Rock Mech. in Petr. Eng. Conf., The Netherlands, August 29-31.
- Lewan, M. D., 1987, Petrographic study of primary petroleum migration in the Woodford Shale and related rock units: in *Migration of hydrocarbons in sedimentary basins* (ed. B. Doligez), IFP Exploration Research Conference: 45, 113 – 130.
- Meissner, F.F., 1978, Petroleum Geology of the Bakken Formation Williston Basin, North Dakota and Montana: Williston Basin Symposium, The Montana Geological Society 24th Annual Conference, Billings, Montana.
- Mraz, T., DuBow, J., and Rajeshwar, K., 1983, Acoustic wave propagation in oil shale, *FUEL*, Vol 62, 1215 – 1222.
- Passey, Q.R., Creaney, S., Kulla, J.B., Moretti, F.J., Stroud, J.D., 1990, *AAPG Bull.*, v. 74, no. 12, 1777-1794.
- Prasad, M., 2001, Mapping impedance microstructures in rocks with acoustic microscopy: *The Leading Edge*, 20: 172 – 179.
- Prasad, M., Reinstädler, M., Nur, A., and Arnold, W., 2002a, Quantitative acoustic microscopy: Applications to petrophysical studies of reservoir rocks, *Kluwer Publications, Acoustical Imaging* 25: 381-387.
- Prasad, M., Kopycinska, M., Rabe, U., and Arnold, W., 2002b, Measurement of Young's modulus of clay minerals using Atomic Force Acoustic Microscopy, *GRL*, Vol. 29, #8, 13-1 – 13-4.
- Smith, J. W. and Chong, K. P., 1984, *Mechanics of Oil Shale* (eds. Chong K.P. and Smith J.W.), Elsevier Applied Science Publishers.
- Vernik L. and Nur, A., 1994; Ultrasonic velocity and anisotropy of hydrocarbon source rocks: *Geophysics*, 57: 727 – 7351.
- Vernik, L. and Landis, C., 1996, Elastic anisotropy of source rocks: Implications for hydrocarbon generation and primary migration: *AAPG Bull.*, 80: 531 – 544.
- Vernik, L. and Liu, X., 1997, Velocity anisotropy in shales: A petrophysical study: *Geophysics*, 62: 521 – 532.
- Weller, M., and Wert, C.A., 1983; Internal friction of coals and of other natural macromolecular solids: *Jour. de Physique, Colloque C9*, suppliment au n012, Tome 44, C9-191-C9-196.

Wert, C.A., and Weller, M., 1982; Polymeric character of coals: *J. Appl. Phys.*, v. 53, no. 10, 6505-6512.
Zeszotarski, J.C., Chromik, R.R., Vinci, R.P., Messmer, M.C., Michels, R., and Larsen, J.W., 2004, Imaging and mechanical property measurements of kerogen via nanoindentation: *Geochimica et Cosmochimica Acta*, Vol. 68, No. 20, 4113-4119.